Journal of Energy Storage 168 (2026) 122415

Contents lists available at ScienceDirect

Journal of Energy Storage

journal homepage: www.elsevier.com/locate/est

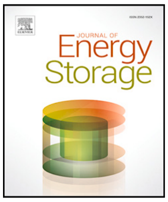

Research Papers

Aging behavior of commercial 18650 sodium-ion cells revealed by non-destructive impedance-derived parameters and post-mortem analysis

Elisa Irujo [a,1], Alberto Berrueta [a,1], Moritz Fabian Schütte [b,c,d,1], Heinrich Ditler [b,c,d], Christiane Rahe [b,c,d], Dirk Uwe Sauer [b,c,d,e], Pablo Sanchis [a], Alfredo Ursúa [a,*]

[a] *Institute of Smart Cities (ISC), Department of Electrical, Electronic and Communications Engineering, Public University of Navarre (UPNA), Campus de Arrosadia, Pamplona, 31006, Navarre, Spain*
[b] *Chair for Electrochemical Energy Conversion and Storage Systems, Institute for Power Electronics and Electrical Drives (ISEA), RWTH Aachen University, Campus-Boulevard 89, Aachen, 52074, Germany*
[c] *Juelich Aachen Research Alliance, JARA-Energy, Jülich, 52425, Germany*
[d] *Center for Ageing, Reliability and Lifetime Prediction of Electrochemical and Power Electronic Systems (CARL), RWTH Aachen University, Campus-Boulevard 89, Aachen, 52074, Germany*
[e] *Helmholtz Institute Münster (HIMS), IMD-4, Forschungszentrum Jülich, Jülich, Germany*

ARTICLE INFO

Keywords:
Aging
Post-mortem
Performance
Sodium-ion battery
Electrochemical impedance spectroscopy
Sodium plating

ABSTRACT

The rapid expansion of energy storage needs and concerns over lithium availability have renewed interest in sodium-ion batteries (SIBs) as a complementary technology to lithium-ion systems. Yet, systematic studies on their aging analysis strategies with the aim of detecting aging indicators remain limited. In this study, we present a comprehensive aging analysis, combining non-destructive electrochemical impedance spectroscopy (EIS) with equivalent circuit model (ECM) parameter tracking and post-mortem analysis. Tracking the longitudinal evolution of ECM-derived parameters demonstrates their utility as aging indicators. Post-mortem and elemental mapping analysis provides mechanistic support for the impedance trends, focusing on characterizing aging mechanisms from a morphological perspective. The methodology is applied to a commercial 1.3 Ah 18650 SIB with a layered-oxide cathode and hard carbon anode at an early-stage development showing a short life cycle of 500 cycles to reach a SOH of 50%, but slower capacity fade under calendar remaining over a SOH of 90% after more than 600 days. ECM parameters show consistent evolution with SOH and aging mechanisms occurring inside the battery observing correlations valuable for potential aging indicators. Post-mortem and elemental mapping confirm sodium plating on the anode surface even in pristine cells. The study clarifies their compositional and morphological evolution through aging. Notably, the study investigates cells down to <60% SOH, a range rarely reported in the literature. The methodology proposed here establishes a replicable framework for monitoring degradation and evaluating aging indicators in sodium-ion batteries, facilitating comparative studies across early-stage cells and supporting the design of improved future generations.

1. Introduction

The global transition towards renewable energies and electric mobility requires storage technologies that are affordable, sustainable, and safe. Although lithium-ion batteries (LIBs) dominate the energy storage market due to their high performance and maturity [9], their growing demand intensifies concerns over lithium scarcity and overall sustainability [10]. As a result, SIBs have positioned as one of the most promising candidates for next-generation storage systems due to the abundance of sodium [11], the continuous development of SIBs elements [12], and similarities with LIBs that allow the direct repurposing of the existing LIBs manufacturing infrastructure for sodium-ion technology [13]. Multiple companies are actively pursuing optimized designs and materials, with hard carbon dominating as the anode and layered oxides, phosphates, and Prussian blue analogues as the main cathode families [14].

In this context, the launch of the first commercial cells has provided a valuable opportunity to conduct performance evaluation and benchmarking against established lithium-ion counterparts. Early investigations are key to identify first weaknesses. Leveraging the transferability of established LIB characterization techniques, these batteries have

---

[*] Corresponding author.
E-mail address: alfredo.ursua@unavarra.es (A. Ursúa).
[1] These authors contributed equally.

https://doi.org/10.1016/j.est.2026.122415
Received 3 December 2025; Received in revised form 1 April 2026; Accepted 22 April 2026

Table 1
Summary of aging analysis studies on commercial sodium-ion batteries.

Ref.	Aging conditions	Min SOH	Diagnostic techniques	Purpose
[1]	Cycle	65%	Capacity and pulse resistance tracking, DVA	Aging modes identification. Comparison of SIBs.
[2]	Calendar	98%	Capacity and Coulombic efficiency tracking, DVA, end-point slippage, post-mortem	Aging modes identification and self-discharge. Comparison of SIBs and LIBs.
[3]	Cycle, Calendar	90%	Capacity, voltage and EIS tracking, ICA, post-mortem	Aging mechanisms characterization.
[4]	Cycle	87%	Capacity, EIS and ECM parameters tracking, ICA, post-mortem	Aging mechanisms characterization and temperature-resistant SOH indicators construction
[5]	Cycle, Calendar	75%	Capacity and pulse resistance tracking, ICA, DVA	Aging modes identification. Gas-induced current interrupt failure.
[6]	Cycle	Severe capacity fade	Capacity, EIS and ECM parameters tracking, ICA, DVA, post-mortem	Aging mechanisms characterization at low-temperature.
[7]	Cycle	80%	Capacity, OCV, pulse resistance and EIS tracking, ICA, post-mortem	Aging modes and mechanisms characterization. Comparison of SIBs and LIBs.
[8]	Cycle	68%	Capacity, pulse resistance, OCV and EIS tracking, DMA	Electrode-resolved aging modes identification.

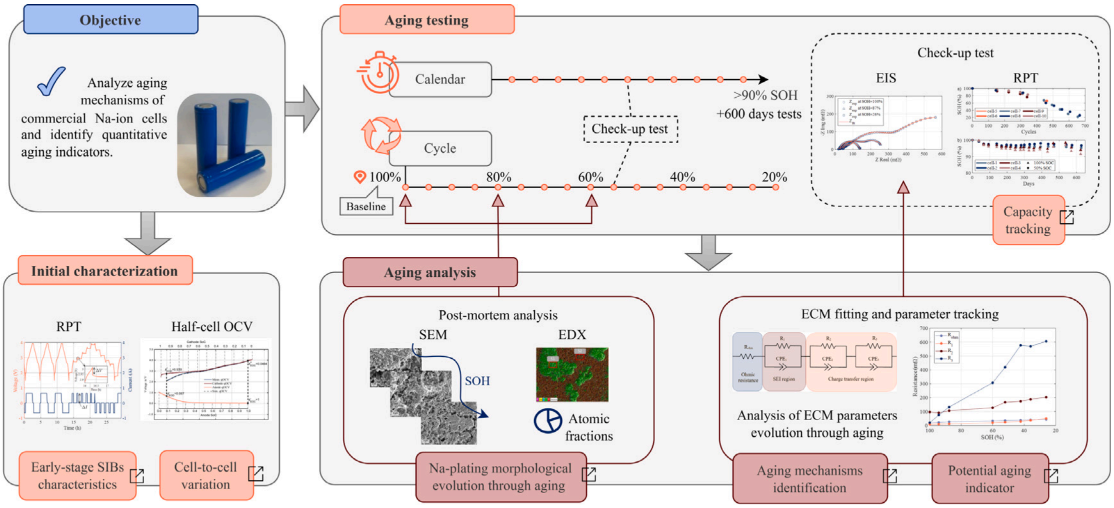

Fig. 1. Methodological workflow of the paper aging analysis, illustrating the combined approach based on experimental aging, post-mortem characterization, and impedance analysis through ECM modeling, and highlighting the resulting outputs and contributions.

been studied from diverse angles. Regarding structural aspects, electrochemical analysis reveals that many commercial SIBs employ layered oxide cathodes [1], confirming a design concept nearly identical to that of conventional LIBs [15]. The electrical performance of these SIBs has been extensively investigated under different operating conditions, including variations in temperature, C-rate [1], and state of charge (SOC) [16]. Equivalent LIBs characterization methods along with post-mortem analysis confirm SIBs potential in terms of rate capability and thermal behavior [17] and similar characteristics to LIBs regarding fundamental parameters [18]. Cycle life characterization in these studies reveals significant differences in aging behavior. Some commercial cells retain nearly full capacity over 1000 cycles [1,17], whereas others decline to 80% SOH after only 300–400 cycles [1,18].

Understanding and characterizing SIBs aging is essential for further technology development, as degradation depends on the battery technology [19]. There are non-destructive and post-mortem techniques that provide valuable information about aging. Non-destructive techniques include incremental capacity analysis and differential voltage analysis, impedance analysis based on electrochemical impedance spectroscopy (EIS) and distribution of relaxation times. Post-mortem techniques commonly employed include physical disassembly, morphological characterization via scanning electron microscopy (SEM) and energy-dispersive X-ray spectroscopy (EDX), and chemical analytical techniques. In LIBs, numerous studies have shown that these techniques not only reveal degradation modes and mechanisms, such as loss of cyclable lithium, solid-electrolyte interphase (SEI) growth, and electrode structural changes [20], but that the tracking of parameters derived from these techniques can serve as SOH indicators [21–23].

Although SIBs share many fundamental electrochemical processes with LIBs, the validity of applying the same aging analysis techniques and SOH estimation approaches to SIBs must be carefully verified. Systematic degradation analyses in commercial SIBs are still scarce, particularly those combining non-destructive techniques with post-mortem validation to track parameter evolution. Recent studies have begun to address this gap and Table 1 provides an overview of the literature on the aging analysis of commercial SIBs. Most of the existing studies focus primarily on qualitative analyses aimed at identifying the dominant degradation modes and the key mechanisms responsible for capacity fade and impedance growth. These investigations generally monitor cells that retain relatively high states of health (SOH > 60%), limiting the understanding of aging behavior under more severe conditions. To date, only one study performed an aging analysis to commercial SIBs from a quantitative perspective and with the purpose of identifying indicators for SOH estimation [4]. The work combines multiple indicators derived from impedance measurements to train a support vector regression model for SOH estimation. While

Nomenclature

Acronyms & Abbreviations

CC	Constant current
CPE	Constant phase element
CV	Constant voltage
DOD	Depth of discharge
ECM	Equivalent circuit model
EDX	Energy-dispersive X-ray spectroscopy
EIS	Electrochemical impedance spectroscopy
EOL	End of life
GITT	Galvanostatic intermittent titration technique
LIB	Lithium-ion battery
OCV	Open circuit voltage
RPT	Reference performance test
SEI	Solid-electrolyte interphase
SEM	Scanning electron microscopy
SIB	Sodium-ion battery
SOC	State of charge
SOH	State of health

this approach shows the potential of EIS-derived indicators, it does not provide a detailed longitudinal analysis of ECM parameters nor validate their physical relevance as quantitative aging indicators across deep aging, which is the focus of the present work.

The present work presents a comprehensive framework for aging analysis of sodium-ion batteries by combining longitudinal ECM-based impedance parameter tracking trough aging with post-mortem analysis, as illustrated in Fig. 1. The methodology is applied to a commercial 18 650 cells with layered-oxide cathodes and hard carbon anodes providing also its electrical characterization and aging behavior under calendar and cycle aging. Moreover, the post-mortem analysis in this work captures sodium plating, previously observed in commercial sodium-ion cells under few cycles and high C-rates [24,25], but here its morphological evolution is analyzed during extended cycling down to 60% SOH. This results offer a comprehensive evaluation of this SIB technology and provide mechanistic insight rarely accessible in early-generation cells.

2. Experimental setup

2.1. Cell description

The cell studied herein is a SIB in a cylindrical 18 650 format commercialized by Tycorun Energy Co., Ltd [26]. It is model 18650E-1300 with hard carbon as anode and layered transition metal oxide as cathode. Its nominal capacity is 1.3 Ah and the nominal voltage is 3.1 V. The maximum and minimum operating voltages in charge and discharge are 3.95 V and 1.5 V. The maximum charging and discharging currents are 1 C and 3 C, respectively. The operating temperature ranges from −10 to 45°C in charge and from −30 to 60°C in discharge. Finally, the cell mass is 30 ± 0.5 g, leading to an energy density of 118 Wh/kg.

2.2. Characterization testing techniques

The following reference performance test (RPT) with four steps is proposed for the electrical characterization of a SIB.

1. Three full cycles with a CC-CV charge at 0.5 C with cut-off voltage of 3.95 V and cut-off current of 0.05 C. The discharge is CC at 0.5 C with cut-off voltage of 1.5 V.
2. Galvanostatic intermittent titration technique (GITT) in charge and discharge at 0.5 C by pulses of ΔSOC = 20% and rests of 1 h within.
3. Pseudo-OCV technique at C/20.
4. Charge the cell to $SOC = 50\%$.

The Electrochemical Impedance Spectroscopy (EIS) technique is used to measure the impedance at a SOC of 50% within the frequency range from 50 mHz to 30 kHz. In this paper, the combination of RPT and EIS is referred to as the check-up test.

2.3. Calendar aging experiment

The calendar aging experiment is performed at a controlled temperature of 25 ± 3°C and the desired SOC level. The cells are stored during around 30 days on the shelf. After this calendar time, a check-up test (as described above) is performed, and the cell is returned to the shelf for a subsequent calendar period.

2.4. Cycle aging experiment

The cycle aging experiment is also performed at a controlled temperature of 25 ± 3°C, full cycles of DOD = 100%, CC-CV charge and CC discharge at 0.5 C with a voltage range of 1.5 V–3.95 V and a cut-off current of 0.05 C.

After a number of cycles between 50 a 100, the cycling profile is stopped, and the cells are characterized by means of the check-up test described above. Afterwards, a new cycling set starts.

2.5. Post-mortem analysis

The cells are discharged to their end of discharge voltage using a current of 0.05 C. Afterwards, the cells are opened in a glovebox under an argon atmosphere. The cell casing was first cut circumferentially at the positive terminal using a pipe cutter, then carefully peeled away with pliers. Afterwards, the electrodes were separated without short-circuiting by unrolling the jelly roll. The electrodes are scanned inside the glovebox. The electrodes are also examined by means of optical microscopy, as well as by Scanning electron microscopy (SEM) and energy-dispersive X-ray spectroscopy (EDX).

Coin cells for half-cell electrical characterization are assembled using CR2032 housings. The assembly process begins by placing a single-side coated electrode, with a diameter of 16 mm, inside one part of the housing. Single-sided coating was obtained by mechanically removing the active material from one side using a ceramic knife inside the glovebox. A 17 mm diameter separator (Whatman GF/C) is then positioned and saturated with electrolyte. For each coin cell, 90 μL of electrolyte (1.2 M $NaPF_6$ in EC:PC 1:1 by weight) is added. A sodium metal chip is then placed on top of the separator. The sodium metal chip (diameter of 15.6 mm, AOT Battery) is composed of a 30 μm aluminum layer, and a 420 μm sodium layer. To improve electrical contact, a stainless steel spacer and a spring are incorporated.

Anode and cathode coin cells are cycled at rates of C/50 and C/100 with 1 h between charging and discharging, respectively. The anode coin cell is cycled between 0.01 V and 1.5 V, while the cathode is cycled between 2.0 V and 4.05 V. Higher C-rates are not included due to the problems related to overvoltage vs. sodium metal discussed by Laufen et al. [17].

2.6. Experimental matrix

The experimental matrix is designed in order to allow a comparison of the initial characteristics of the Na-ion cells, as well as a comparative analysis of the calendar and cycle aging effect. Table 2 shows the experiments performed with each of the 12 cells. As shown in the second column, all the pristine cells are characterized by means of the RPT detailed above. 10 of the cells are aged; under calendar effect (cells 1 to 4) at different SOC levels, as well as under cycle conditions (cells 5 to 10). All the aging experiments are done at an ambient temperature

Table 2
Experimental matrix of 12 Na-ion cells. All the experiments are performed at a temperature of 25 ± 3°C.

Cell #	Initial RPT	Aging	EOL	Post-mortem
1	✓	Cal. SOC = 50%	–	–
2	✓	Cal. SOC = 50%	–	–
3	✓	Cal. SOC = 100%	–	–
4	✓	Cal. SOC = 100%	–	–
5	✓	Cycle	SOH = 60%	✓
6	✓	Cycle	SOH = 60%	✓
7	✓	Cycle	SOH = 10%	–
8	✓	Cycle	SOH = 10%	–
9	✓	Cycle	SOH = 80%	✓
10	✓	Cycle	SOH = 80%	✓
11	✓	No aging	–	✓
12	✓	No aging	–	✓

Fig. 2. Experimental setup, consisting of a battery tester and a thermal chamber, in the Laboratory for Energy Storage and Microgrids of the Public University of Navarre (UPNA).

of 25 ± 3°C. Given that calendar aging is a slow process, no end of life (EOL) criteria is required. By contrast, two of the cycled cells are removed from the experiment when they reach SOH = 80%, other two cells are removed at SOH = 60%, and the remaining two cells are cycled until SOH = 10%. The post-mortem study is done with four cycled cells and with two pristine cells to allow a comparative analysis.

2.7. Testing equipment

On the one hand, the aging experiments and electrical characterization techniques of this contribution are performed in the Laboratory for Energy Storage and Microgrids of the Public University of Navarre (UPNA). A battery tester manufactured by Neware is used for RPT, check-up and cycle tests, as appreciated in Fig. 2. Each channel allows a maximum voltage and current of 5 V and 12 A whose precision is ±0.05% in current measurement. The EIS are obtained using PSM3750 Frequency Response Analyzer, which ranges from 10 μHz to 50 MHz.

On the other hand, the post-mortem analysis is performed at the Institute for Power Electronics and Electrical Drives (ISEA) of the RWTH Aachen University. A Neware CT-4008T-5V10 mA battery cycler is used for half-cell voltage determination (0.05% FS accuracy). The glovebox used for this study is a MBRAUN LABstar (O_2 concentration < 0.5 ppm, H_2O concentration < 0.5 ppm). The electrodes are scanned using a Canon CanoScan LiDE 300 flatbed scanner at a resolution of 600 DPI. For the optical microscopy studies, a Keyence VKX1100 is utilized. The SEM analysis is conducted using a Zeiss Supra 55, equipped with an SE detector and operating at an accelerating voltage of 5 kV. Finally, an Oxford Instruments Ultim Extreme detector was used for the EDX analysis.

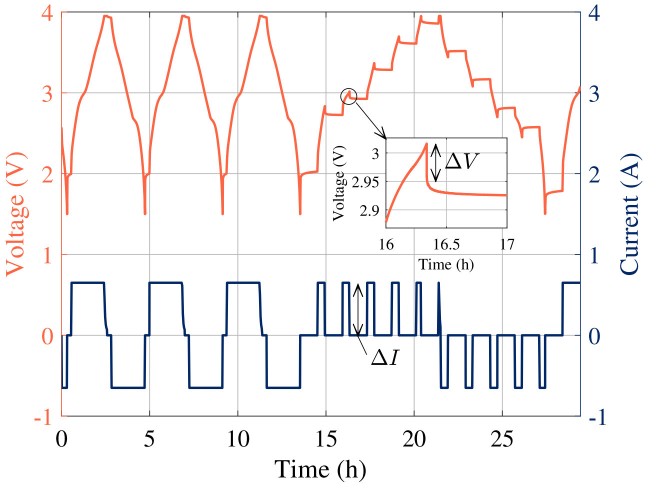

Fig. 3. Voltage and current profiles for steps 1 and 2 of the Reference Performance Test. Zoom graph shows the voltage response to a current step, performed to obtain the internal resistance (R_i).

3. Characterization of pristine Na-ion cells

All Na-ion cells were initially characterized by the procedure aforementioned in Section 2.2 in order to evaluate cell-to-cell variation and obtain fundamental parameters. The profile of the test with the voltage response is shown in Fig. 3. In the last cycle of the three full cycles performed in step 1 of RPT, the charged energy (E_{ch}), the discharged capacity (C_{ini}) and the discharged energy (E_{dch}) are measured. The energy efficiency (η_E) is computed as follows:

$$\eta_E = \frac{E_{dch}}{E_{ch}} \tag{1}$$

Values of C_{ini}, in blue asterisk, for the 12 cells are represented in Fig. 4(a), alongside the normal distribution of the data to characterize cell-to-cell variation and the nominal capacity shown in orange. Considering the 12 samples, the measured average discharge capacity is 1.20 ± 0.05 Ah (95% CI), which corresponds in average to the 92.31% of the nominal capacity declared by the manufacturer. Fig. 4(b) shows the values obtained for η_E, in blue asterisk, along with the normal distribution. When it comes to the energy efficiency, these SIBs present 91.79 ± 2.05% (95% CI) in average.

Fig. 5 reveals the internal resistance (R_i) calculated in the rests of GITT performed in step 2 of RPT during charge and discharge at SOCs of 20%, 40%, 60% and 80%. The internal resistance is computed according to Ohm's law as:

$$R_i = \frac{\Delta V_{10s}}{\Delta I_{10s}} \tag{2}$$

where ΔI corresponds to the charging or discharging current pulse and ΔV the voltage response generated in following 10 s, as indicated in Fig. 3. A higher degree of variability is observed in the charge resistances, particularly at 20% and 40% SOC, where the interquartile

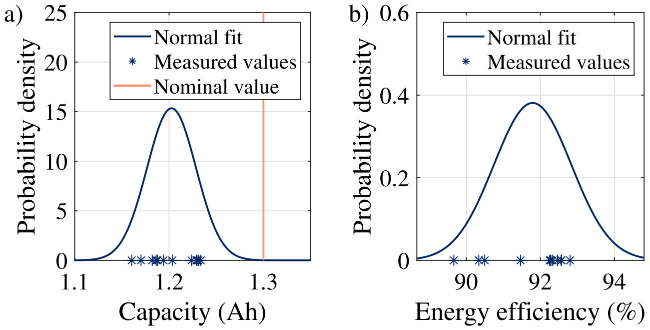

Fig. 4. Experimental values and normal distribution of the: (a) discharge capacity and (b) energy efficiency of pristine cells.

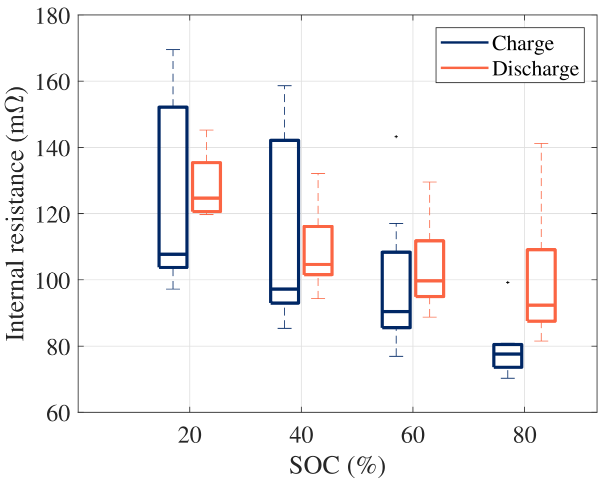

Fig. 5. Boxplot representation of the internal resistance measured across the SOC range for pristine cells, distinguishing between charge and discharge conditions.

range (IQR) reaches a value of 48.77 mΩ. The rest of boxplots depicted show lower IQR with an average value of 16.24 mΩ. Comparison between charge and discharge reveals that resistances during discharge are about 10.91% and 29.25% higher than during charge at SOCs of 60% and 80%. The influence of the SOC in the internal resistance can be appreciated in Fig. 5 with the downward trend as the SOC increases. In average among the 12 samples, the internal resistance measured in the charge at a SOC of 80% is 88.6 mΩ, which corresponds to 70.56% of the average internal resistance obtained for a SOC of 20%. Additional electrical test analysis of same SIBs model is provided in [18], along with a comparison with equivalent LIBs.

Lastly, the equilibrium OCV measured at C/100 in half-cell configuration is presented herein for deeper analysis of the OCV-SOC relationship. Half-cell OCV measurements provide the individual anode and cathode voltage characteristics vs. Na/Na^+, enabling separation of electrode-specific contributions that are inaccessible in full-cell measurements. The top graph of Fig. 6 presents the OCV dependency on SOC. Both half-cell voltages of the anode and cathode have been measured by a coin cell, and the results are presented in maroon color (cathode) and orange color (anode) in the figure. The measured cathode OCV has a reduced slope for SOC < 0.4, while the slope increases for larger SOCs. By contrast, the anode OCV has a large slope for a full cell SOC < 0.3, it reaches a value close to 0 V vs. Na/Na^+, and has a reduced slope for higher full cell SOCs. The full cell OCV is provided by the subtraction of cathode and anode OCV. The top graph of Fig. 6 shows the calculated full-cell OCV in black, dashed line, and the measured full cell OCV during a C/20 CC-charge in blue, full line. The

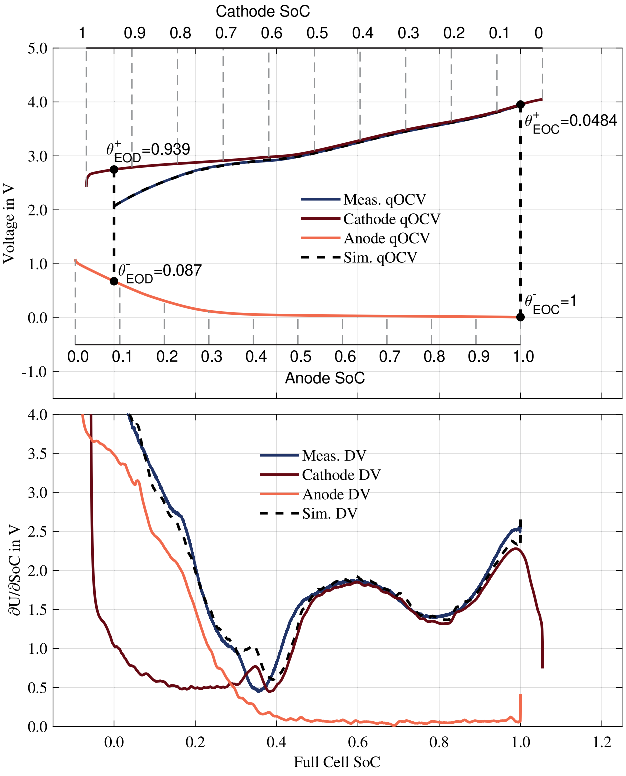

Fig. 6. Open-circuit voltage analysis of half cells and full cell: open circuit voltage (top) and differential voltage (bottom).

calculation and measurement are virtually superimposed, resulting in a RMSE of 6.1 mV. The fitting was done in the same way as in Schütte et al. [27]. The OCV-SOC relationship has a consistent slope along the whole SOC, with a voltage change minima around SOC ≈ 0.35, which is something to be taken into account for analyses such as the SOC estimation.

The bottom graph of Fig. 6 shows the differential voltage $\left(\frac{\partial U}{\partial SoC}\right)$ of both half cells and of the full cells. Large differential voltage are measured in both electrodes for low values of SOC, while its value is limited to 2.5 V for SOC > 0.2. The voltage plateau described in the previous paragraph is represented with a minimum differential voltage of 0.5 at SOC ≈ 0.35, and a relative maximum of 1.8 V is detected at SOC ≈ 0.6. This differential voltage analysis provides more detailed information about the slope of the OCV curve. Differential voltage analysis reveals the relationship between anode and cathode contributions to the overall cell voltage. The analysis elucidates the slope characteristics of the OCV curve. Given that the anode operates close to its plating limit at 0 V vs. Na/Na^+ at the end of charge, a fitting factor of 1 for the anode half cell indicates either a high risk of sodium plating or, alternatively, a systematic limitation in the measurement methodology of the half cell voltage characterization. Half cell voltage measurements provide insights into changes in entropy coefficients, offering valuable perspectives for future research [28]. The half-cell voltage profiles closely resemble those of hard carbon and $NaNi_{1/3}Fe_{1/3}Mn_{1/3}O_2$ materials reported by Schütte et al. [27] and Rehm et al. [16].

4. Equivalent-circuit representation of a Na-ion cell

The internal resistance R_i shown in Fig. 5 can be further expressed as a complex impedance, which provides a valuable tool for assessing the aging processes that affect the operation of a SIB. Following the approach commonly adopted for lithium-ion batteries [21], the

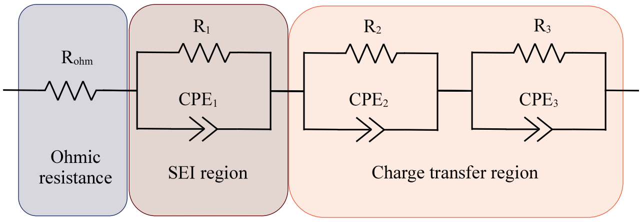

Fig. 7. Equivalent circuit model used to fit the impedance experimental data.

impedance of the cell is represented by an ohmic resistance (R_{ohm}), which accounts for the resistance of the electrolyte, separator, and current collectors, together with parallel branches of resistances and constant phase elements (CPEs) to capture the dynamic behavior of the battery. Note that the impedance of a CPE is given by:

$$Z_{CPE} = \frac{1}{Q(j\omega)^n} \tag{3}$$

where ω is the angular frequency, Q and n are the characteristic parameters of the CPE. The value of n is bounded between 0 and 1. The time constant of the $R_i \parallel CPE_i$ circuit can be calculated as follows [29]:

$$\tau_i = (R_i \cdot Q_i)^{\frac{1}{n}} \tag{4}$$

The selected equivalent circuit model was chosen based on its ability to accurately reproduce the experimental impedance response while maintaining physical consistency and minimizing overparameterization, as depicted in Fig. 7. The first branch, $R_1 \parallel CPE_1$, may account for the influence of the SEI on the anode surface, with a differentiated small semicircle in EIS curve at a higher characteristic frequency of around 800 Hz, as done for LIBs. Previous studies have shown that the SEI formed on hard carbon in SIBs exhibits chemical composition and ionic transport behavior analogous to that in LIBs [30–33]. This assignment is supported by its short relaxation time and is consistent with previous studies on SIBs [3,6,34].

At lower frequencies, within 0.15–300 Hz range, the $R_2 \parallel CPE_2$ and $R_3 \parallel CPE_3$ branches describe the charge transfer reaction and electrochemical double-layer phenomena occurring at the electrode/electrolyte interfaces. The use of two $R \parallel CPE$ elements in this frequency region was necessary to account for multiple electrochemical processes with partially overlapping time constants, as indicated by the depressed and asymmetric semicircle in the Nyquist plot through aging. A single charge transfer element could not adequately reproduce this behavior without compromising the fitting quality. The electrochemical processes occurring at lower frequencies than 0.15 Hz typically corresponds to ionic diffusion process and requires prolonged stabilization periods, extended acquisition times, and highly stable experimental conditions to accurately capture true low-frequency impedance [21,35,36]. However, the accurate modeling of diffusion processes is out of the scope of this study.

It should be highlighted that ECMs provide a simplified electrical representation in which each element is assigned to the predominant process within a given frequency range. However, due to these inherent simplifications, each element may also account for secondary or overlapping processes with similar time constants.

5. Electrical aging analysis of Na-ion cells

5.1. Capacity fade

The most typical variable to analyze aging is the state of health, which can be defined by the following expression:

$$SOH = \frac{C_a}{C_{ini}} \cdot 100\% \tag{5}$$

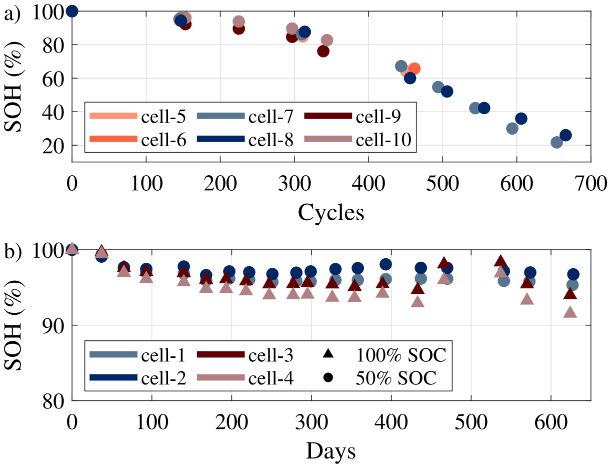

Fig. 8. State of health evolution in: (a) cycle aging and (b) calendar aging.

where C_{ini} refers to the initial capacity and C_a corresponds to the actual capacity measured in each intermediate RPT between aging phases. The SOH evolution of the six cells under cycle conditions is represented in Fig. 8(a). All of them are fully cycled with same conditions, but the SOH results obtained present certain dispersion, which increases with aging. Considering average SOH and number of cycles values, the cell loaded with full cycles degrades at speed of 0.043%/cycle in first 300 cycles. After reaching a SOH of 80%, the curve tendency changes to a steeper slope of 0.133%/cycle, and it only takes 110 cycles more to reach a SOH of 65%. Therefore, the EOL criteria for Na-ion cells should be placed at a SOH close to 80%, similar to Li-ion cells. Fig. 8(b) illustrates the aging of the cells under calendar conditions. After 628 days, the cells stored at SOC of 50% experience a capacity loss of 4%, while the cells at 100% shows a 7.23% reduction. In first check-up measurement, the capacity fade speed was greater, which is associated to SEI formation and, afterwards, the calendar aging speed is of 0.0026%/day for the cells stored at a SOC of 50% and 0.0072%/day for the cells stored at full charge. The influence of SOC increases with time, with a 80.75% more degradation at storage SOC of 100% than the one suffered at 50%.

5.2. Impedance rise

In order to assess the degradation phenomena that dominate cell aging along the lifetime of the cell, the experimental data obtained from the EIS measurements are fitted to the ECM presented in Section 4. The experimental data of three EIS experiments at SOH ranging from 100% to 26% are shown in Fig. 9. As appreciated in the figure, the three arcs corresponding to the three $R \parallel CPE$ branches are easier to distinguish in the measured impedance of the aged cell, being superimposed for the pristine cell. The main effect of the Na-ion cell aging is appreciated in the $R_3 \parallel CPE_3$ with the lower characteristic frequency.

To assess the robustness of the ECM fitting to experimental EIS data, the Mean Relative Error (MRE) between the model-predicted impedance, Z_{fit}, and the measured impedance, Z_{exp}, was computed across all frequencies in the spectrum. This metric provides a relative, frequency-resolved measure of the discrepancy between the ECM and experimental data, allowing a quantitative evaluation of the fitting performance under different SOH [37]. The MRE is defined as

$$MRE = \frac{1}{N}\sum_{i=1}^{N}\frac{|Z_{fit,i}| - |Z_{exp,i}|}{|Z_{exp,i}|} \cdot 100\% \tag{6}$$

where N denotes the total number of frequency points considered.

Fig. 10(c) presents the computed MRE for different SOH levels. It is observed that all relative errors remain below 2.08% across all SOH

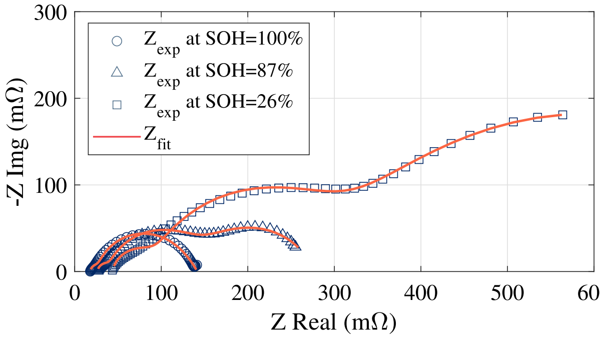

Fig. 9. Impedance measurements via EIS and the impedance modeled with the ECM.

levels, indicating that the ECM provides a high-fidelity representation of the battery impedance and that the fitting procedure is robust irrespective of the battery's state of health.

Fig. 10(a) and (b) shows the evolution of the model resistances and time constants along the battery degradation. The resulting values for the four resistances show growing trend over the course of aging. R_{ohm} multiplies its value by 2.4 after a capacity loss of 74%, attributed to corrosion of current collectors and changes in electrolyte as a result of side reactions, which contributes to conductivity loss. The decrease of ionic conductivity of the electrolyte is likely caused by its reaction with plated sodium to regenerate the SEI layer. The formation of films involving thickness and morphology changes leads to loss of sodium inventory and is reflected in R_1 increase. Both resistance rises can be used as indicators of sodium plating, as explained in [38] for lithium plating detection techniques. In order to further investigate the sodium plating, in Section 6, scanning electron microscopy and energy-dispersive X-ray spectroscopy are used to analyze this aging mechanism. The charge transfer resistances exhibit a more notable increase that can be associated to the decrease of charge transfer during sodium-ion de-/intercalation reaction. Aging mechanisms responsible for the R_2 and R_3 increase are the continuous SEI regeneration due to severe sodium plating creating a metallic cover layer [1], which leads to loss of sodium inventory and loss of active material in the anode. In the cathode, the combination of possible structural disorders and the suggested particle cracking in similar cells in [1] can account for the resistance increase. The increasing evolution of R_3 reveals a clear monotonic and approximately linear relationship with the SOH. This visual trend suggests that R_3 may serve as a potential indicator of the evolution of SOH.

To quantitatively assess this relationship, the linear correlation between R_3 and SOH was evaluated using the Pearson correlation coefficient. The analysis yielded a correlation coefficient of $R = -0.989$, indicating an extremely strong negative linear association between both variables and the associated p-value ($p = 3.65 \cdot 10^{-6}$) confirms that the correlation is statistically significant. To further characterize the relationship, a linear regression model was fitted using SOH as the dependent variable and R_3 as the predictor. The resulting model can be expressed as $R_3\ [\text{m}\Omega] = 859.19 - 8.37 \cdot SOH[\%]$, which exhibits a high goodness of fit, with a coefficient of determination $R^2 = 0.977$ meaning that approximately 97.7% of the variability in SOH can be explained by the variation in R_3. Therefore, R_3 serves as a SOH indicator.

The increasing trend occurring in R_3 is well reflected in the higher time constant τ_3, represented along with the other two time constants in Fig. 10(b). Focusing on the time constants for a pristine cell, the average values of τ_1, τ_2 and τ_3 obtained are 0.04, 0.24 and 0.47 s, respectively. Through aging, the charge transfer processes at lower characteristic frequency slow down, while keeping similar kinetics for the others. Broadly, Na-ion cell processes are slower than the analogous processes in Li-ion cells [39–41].

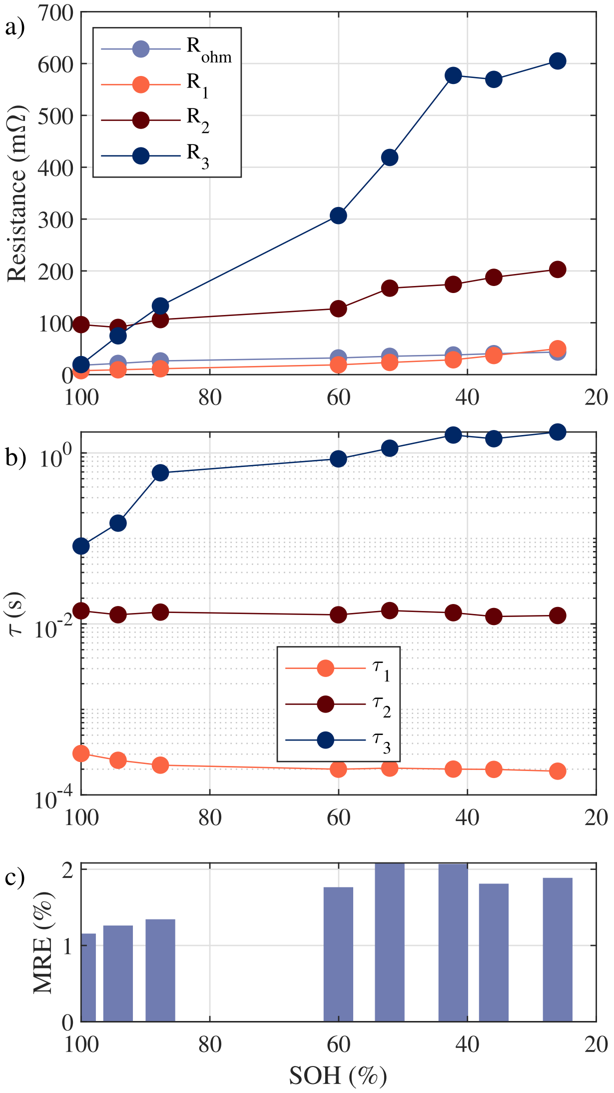

Fig. 10. ECM parameters evolution in aging: (a) resistances and (b) time constants. The MRE at each SOH level is depicted in (c).

6. Post-mortem aging analysis of Na-ion cells

As detailed in Table 2, the post-mortem analysis is done with six Na-ion cells, two of them are fresh pristine cells (Cells 11 and 12), two are at SOH = 80% (Cells 9 and 10) and the other two have a SOH = 60% (Cells 5 and 6). The obtained results are summarized in this section and have focused on characterizing the sodium plating in these Na-ion cells. One cell at each SOH level is selected to showcase the results in this contribution, which are Cells 11, 9 and 5.

The three figures presented in this section (Figs. 11–13) show the material analysis of a new cell (Cell 11), a cell at 80% SOH (Cell 9) and a cell at 60% SOH (Cell 5), respectively. The three figures are divided similarly. The anode scans in the inner and outer radius of the jelly roll are shown on the top part, the results of the EDX analysis and optical microscope images are shown in the central part, while the bottom part is used for SEM images.

The most remarkable characteristic detected in the scan of the anode of the pristine cell, shown in Fig. 11, is a region in the outer radius with apparent sodium plating as zoomed in Fig. 11. Given that the cell has not been cycled after production, this plating is unexpected, and a sample is taken from this area to be compared with a reference non-plated area by means of EDX and SEM analyses.

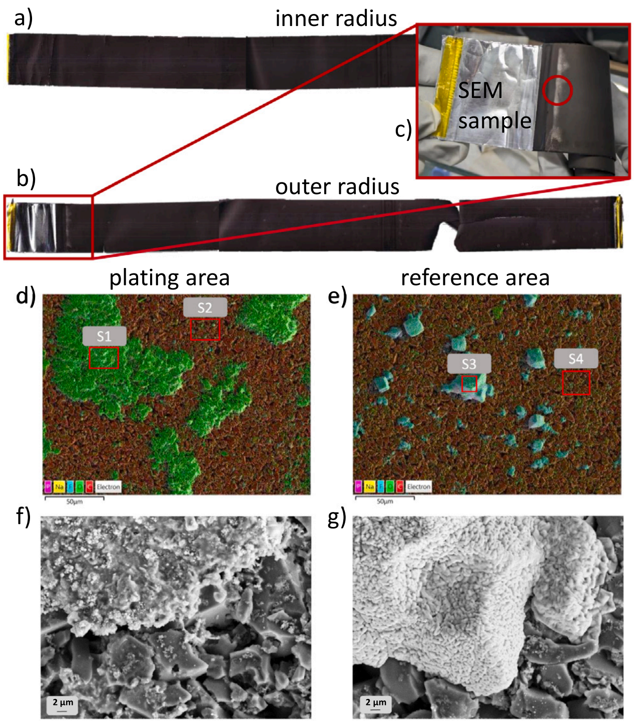

Fig. 11. Anode of fresh Cell 11 (SOH 100%). Anode scans and photo (a, b and c), 500×-zoom 5 kV EDX-map of an area with plated Na (d) and a reference area (e), and 2000×-zoom SEM image of a plating area (f) and a conductive salt agglomeration (g).

Table 3
Atomic fractions of the elements detected by the EDX-sensor in selected samples.

Cell	Sample	SOH (%)	Area	Atomic fraction (%)				
				Na	P	F	C	O
11	Plated Fig. 11(d)	100	Full S1 S2	8.6 20.2 4.4	1.2 3.5 0.5	7.2 22.6 3.0	69.2 26.5 86.4	13.8 26.8 5.5
11	Reference Fig. 11(e)	100	Full S3 S4	4.0 10.6 3.9	1.0 12.1 0.3	6.9 69.6 2.3	83.6 7.1 89.1	4.6 0.6 4.4
9	Fig. 12(e)	80	Full	15.3	2.7	17.0	41.1	23.8
9	Fig. 12(f)	80	Full	16.1	2.9	16.1	38.5	26.4
5	Fig. 13(d)	60	Full	17.4	2.4	12.4	34.6	33.2

Fig. 11(d) presents a 500×-zoom 5 kV EDX map of a region exhibiting plating. Two local EDX spectra are performed in the areas S1 and S2 to confirm that the green area is sodium plating. The results of the EDX are presented in Table 3. The brown area S2 has 4.4% of Na and 5.5% of O, while the green area S1 has 20.2% of Na and 26.8% of O. By contrast, the content of C of S2 is significantly higher than S1 (86.4% vs. 26.5%). This is a clear indicator of sodium plating on the outer side of the jelly roll, next to the anode overhang. Since the cell is new, we postulate an unfavorable formation protocol in the production process. The full area atomic fractions of this sample are in between S1 and S2.

Fig. 11(e) shows a 500×-zoom 5 kV EDX map of a reference area that shows no visible sodium plating. Some small depositions are also visible on the anode. Two areas, S3 and S4, are selected for EDX spectra. Table 3 compiles the results of these measurements. S3 has a substantially higher fraction of F compared to S4 (69.6% vs. 2.3%), which, in combination with approximately 1/6 F fraction in P, confirms the presence of large conductive salt agglomerations and rules out the hypothesis of sodium plating in this anode region.

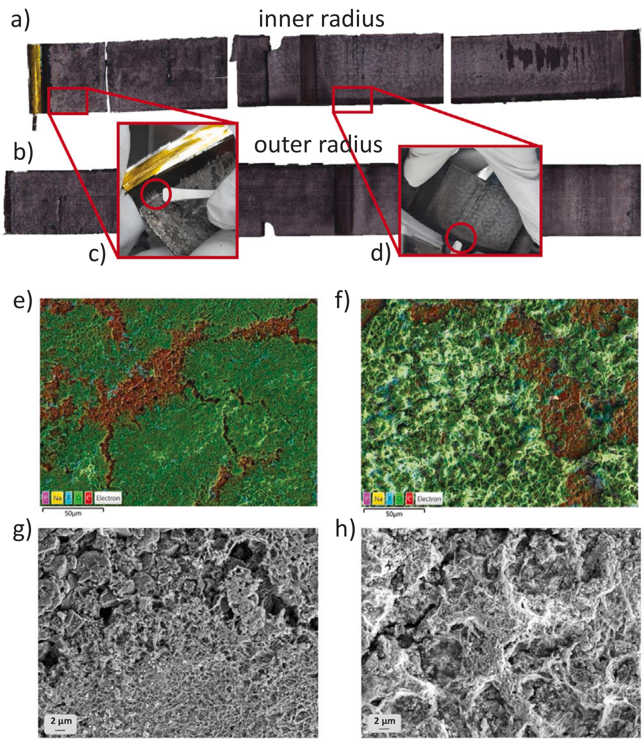

Fig. 12. Anode of Cell 9 (SOH 80%). Anode scans and photo (a, b, c and d), 500×-zoom 5 kV EDX-map of two areas (e and f), and 2000×-zoom SEM images (g and h).

Fig. 11(f and g) display 2000×-zoom SEM images of the areas shown in Fig. 11(d and e). A significant difference in the surface characteristics between sodium plating and conductive salt agglomeration is observed. The hard carbon structure observed in the SEM differs from the spherical structure shown in Mikitisin et al. [42] and is more similar to that in Laufen et al. [17].

The first aging phenomena that occur in a Na-ion cell are studied in Fig. 12, which presents the post-mortem analysis of the anode from Cell 9, with a SOH of 80%. A comparative analysis of the anode scans presented in Fig. 12(a and b), with those of the new cell depicted in Fig. 11 shows a significant increase in sodium plating along the whole surface of the anode, both in the inner and outer radius of the jelly roll. Two samples are taken for a closer SEM analysis, as highlighted with red circles in Fig. 12(c and d). In Fig. 12(c) the sodium plating appears to be migrating towards the direction of the anode overhang.

Fig. 12(e and f) display 500×-zoom 5 kV EDX map of the samples from (c and d), respectively. The sample taken from the surrounding of the anode overhang has a flat and even sodium plating, while the plating on the sample taken from the center of the anode resembles spider-web structures. Table 3 compiles the results of the EDX spectra. In this case, the samples shown in the figure are homogeneous enough to be fully analyzed with no area division. The atomic fractions of the materials found in these two samples are very similar, revealing that, regardless of the plating shape, the aging mechanisms have been homogeneous along the anode. Comparing the elements found in Cell 9 (SOH 80%) with those of the pristine Cell 11, the share of Na has been significantly increased to around 16%, which indicates the importance of sodium plating during this SOH range from 100% to 80%. The share of F and O have been also increased, while C has been reduced, which indicates that the plated Na has been passivated by means of reactions with F and O, thereby reducing the share of hard carbon, which is the actual anode electrode material.

Fig. 12(g and h) present 2000×-zoom SEM images corresponding to the EDX maps illustrated (e and f), respectively. The different surface

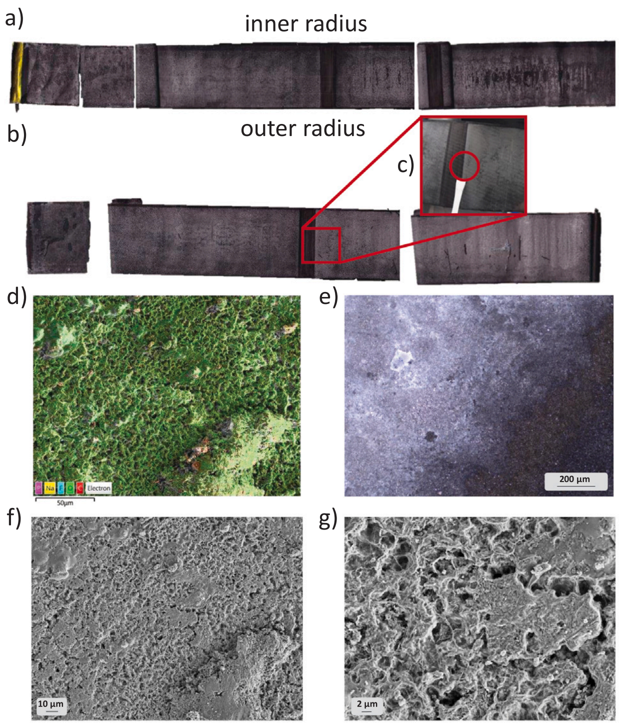

Fig. 13. Anode of Cell 5 (SOH 60%). Anode scans and photo (a, b and c), 500×-zoom 5 kV EDX-map of an area with plated Na (d), 50×-zoom optical microscopy image (e), and 500×-zoom (f) and 2000×-zoom (g) SEM images of a plating area.

characteristics of the flat sodium plating close to the anode overhang and the uneven sodium plating on a regular part of the anode.

The post-mortem analysis of Cell 5 (SOH 60%) is presented in Fig. 13. The anode scans presented in Fig. 13(a and b) are quite similar to those of Fig. 12, which indicates that it is difficult to detect additional sodium plating in the SOH range from 80% to 60%. The sample for the SEM analysis is taken from the opposite site of the area occupied by the cathode current collector, as shown in Fig. 13.

Fig. 13(d) displays the 500×-zoom 5 kV EDX map of the SEM sample, indicating that the sodium plating has increased in the SOH range from 80% to 60%, since there is no hard carbon visible and all of the anode is covered by the plated sodium. The material analysis shown in Table 3 shows a slight increase in the atomic fraction of Na from SOH 80% to 60% coupled with a corresponding decrease in C atomic fraction. Therefore, most of anode surface is already plated from SOH 100% to 80%. This phenomena continues, until the whole surface is covered, from SOH 80% to 60%, when most of the anode surface is covered by plated Na. This could explain the continuous impedance rise observed in Section 5.2, as passivated sodium plating increases both charge transfer and ohmic resistance. Fig. 13(e) presents a 50×-zoom optical microscopy image of the transition area between unused hard carbon and cycled hard carbon, with a clear gradient of plated sodium.

The texture of the plated sodium at SOH 60% is detailed in Fig. 13(f and g), showing 500× and 2000× SEM images, respectively, of the sample shown in (d). The surface characteristics of the fully plated anode are similar to those reported in Fig. 12 for the sodium plated at SOH 80%. The spider-web structure reappears in Fig. 13(g) with localized areas of flattened surface morphology. This may be attributed to pressure constraints within the cylindrical cell geometry, leading to densification of sodium plating in specific regions. Future investigations should examine the influence of pressure, housing conditions, temperature, and C-rate on sodium plating morphology in commercially relevant cell formats.

7. Conclusions

The main contribution of this work lies in the development of a comprehensive aging analysis methodology that combines impedance analysis using an ECM and post-mortem analysis. This integrated approach enables the identification of the evolution of the physical phenomena responsible for SIBs degradation and their potential to serve as aging indicators. Beyond providing a deeper understanding of aging mechanisms in commercial SIBs, the proposed methodology offers a transferable framework for the assessment of other emerging battery technologies.

A prior characterization of the commercial 18 650 SIB is carried out before the aging analysis. The nominal capacity of fresh cells deviates from the manufacturer's specification by an average of 7.7%. Post-mortem observations on pristine cells revealed local sodium plating on portions of the anode surface, indicating an incomplete or non-optimal SEI formation protocol during manufacturing. Salt agglomerations were also detected, a feature commonly reported in lithium-ion batteries. Moreover, the cell-to-cell variations regarding the internal resistance during discharge and during charge are presented. The open-circuit voltage curve displayed a monotonic trend without extended plateau regions, which facilitates state of charge estimation. The dynamic response of the cells throughout their lifetime was well captured by an ECM comprising three $R \parallel CPE$ branches.

Regarding the aging analysis, capacity fade observed during cycling tests indicates a relatively short cycle life, reaching 80% of the initial capacity after approximately 300 cycles. In contrast, cells subjected to calendar aging conditions remained stable for more than 600 days, exhibiting a capacity loss of 4–7.23%, depending on storage SOC. The evolution of the impedance, analyzed through ECM, reveals that each resistance rise can be associated to different aging mechanisms. Charge transfer resistances increases account for different aging processes occurring in the electrodes and serve as valuable early indicator of the drastic SOH drop. At 80% SOH, sodium plating is already present and exhibits various morphologies – from flat layers to spider-web structures – yet with similar elemental composition. Below 80% SOH, further sodium deposition progressively covers the entire electrode surface and the deposited layer thickens, further exacerbating performance losses. Elemental mapping by EDX of Na, C, P and F in plated versus reference areas has provided insights into how the distribution of these elements evolves with aging. Along with other aging mechanisms, the progressive increase in sodium plating with aging can explain the continuous rise in ECM-derived resistances, as passivated sodium deposits contribute to charge transfer, SEI and ohmic resistances rise.

By combining in situ ECM analysis with post-mortem characterization, this study complements and extends the insights available in current literature, providing a deeper understanding of the degradation mechanisms governing early-stage commercial Na-ion systems. Future work should be focused on the application of this aging analysis methodology on further commercial SIBs with different formats and materials to compare their behaviors, which may be different. The results presented in this work serve as a reference for future SIB generations. Moreover, the observed correlation between ECM parameters and aging phenomena opens the door for the construction of advanced SOH indicators.

CRediT authorship contribution statement

Elisa Irujo: Writing – original draft, Software, Methodology, Investigation, Formal analysis, Data curation. **Alberto Berrueta:** Writing – review & editing, Validation, Supervision, Methodology, Investigation, Conceptualization. **Moritz Fabian Schütte:** Writing – original draft, Visualization, Methodology, Investigation, Formal analysis, Data curation. **Heinrich Ditler:** Validation, Methodology, Investigation, Conceptualization. **Christiane Rahe:** Validation, Supervision, Project administration, Funding acquisition. **Dirk Uwe Sauer:** Validation, Supervision, Resources, Funding acquisition. **Pablo Sanchis:** Validation, Resources, Project administration, Funding acquisition. **Alfredo Ursúa:** Validation, Supervision, Project administration, Funding acquisition, Conceptualization.

Declaration of Generative AI and AI-assisted technologies in the writing process

During the preparation of the manuscript, the authors used Perplexity AI to improve readability and language. After using this tool, the authors reviewed and edited the content as needed and take full responsibility for the content of the publication.

Funding

This work was supported by grants PID2022-139914OB-I00 funded by MICIU/AEI/10.13039/501100011033/ (Spain) and by ERDF/EU (European Union), and by PRIDEBAT (PC24-PRIDEBAT-014-002) funded by the Department of University, Innovation and Digital Transformation of the Government of Navarre (Spain). It was also supported by the Federal Ministry for Economic Affairs and Energy (BMWE) of Germany under grant number 03EI6106 (WINTER) and by the Federal Ministry of Research, Technology and Space (BMFTR) of Germany under grant number 03XP0627I (SIB:DE). Elisa Irujo was supported by a predoctoral contract from the Public University of Navarre (Spain).

Declaration of competing interest

The authors declare the following financial interests/personal relationships which may be considered as potential competing interests: The authors declare that they have no known competing financial interests or personal relationships that could have appeared to influence the work reported in this paper.

Data availability

Data will be made available on request.

References

[1] F. Dorau, A. Sommer, J. Koloch, R. Roess-Ohlenroth, M. Schreiber, M. Neuner, K.A. Gamra, Y. Lin, J. Schöberl, P. Bilfinger, S. Grabmann, B. Stumper, L. Katzenmeier, M. Lienkamp, R. Daub, Comprehensive analysis of commercial sodium-ion batteries: Structural and electrochemical insights, J. Electrochem. Soc. 171 (2024) http://dx.doi.org/10.1149/1945-7111/ad7765.

[2] L. Streck, T. Roth, H. Bosch, C. Kirst, M. Rehm, P. Keil, A. Jossen, Self-discharge and calendar aging behavior of li-ion and na-ion cells, J. Electrochem. Soc. 171 (2024) http://dx.doi.org/10.1149/1945-7111/ad6cfd.

[3] W. Li, H. Xie, S. Lin, Y. Qin, J. Zeng, P. Zhang, J. Zhao, Insights on the degradation mechanism of 7 Ah sodium ion batteries at different aging modes, J. Power Sources 639 (2025) http://dx.doi.org/10.1016/j.jpowsour.2025.236635.

[4] Y. Liu, L. Yang, R. Liao, C. Hu, Y. Xiao, C. He, X. Wu, Y. Zhang, S. Li, Degradation mechanism of sodium-ion batteries and state of health estimation via electrochemical impedance spectroscopy under temperature disturbances, Energy 332 (2025) http://dx.doi.org/10.1016/j.energy.2025.137064.

[5] S. Klick, H. Laufen, M. Schütte, B. Qian, K.L. Quade, C. Rahe, M. Dubarry, D.U. Sauer, Failure mode and degradation analysis of a commercial sodium-ion battery with severe gassing issue, Batter. Supercaps 8 (2025) http://dx.doi.org/10.1002/batt.202400546.

[6] Y. Liu, L. Yang, R. Liao, Y. Zhang, S. Li, Study on low-temperature charging aging behavior and degradation mechanism of sodium-ion batteries, J. Energy Storage 124 (2025) http://dx.doi.org/10.1016/j.est.2025.116927.

[7] Z. Zhu, D. Qiao, Y. Huang, J. Zhu, Y. Zheng, Q. Chen, Comparative study of performance and hybrid battery configuration of sodium-ion and lithium-ion batteries, J. Energy Storage 140 (2025) http://dx.doi.org/10.1016/j.est.2025.118904.

[8] M. Rehm, J. Bahrke, J. Natterer, L. Milutinovic, F. Roehrer, A. Jossen, Aging of commercial sodium-ion batteries with layered oxides: how to measure and analyze it? EES Batteries 2 (2026) http://dx.doi.org/10.1039/D5EB00221D.

[9] M.M. Hasan, R. Haque, M.I. Jahirul, M.G. Rasul, I.M. Fattah, N.M. Hassan, M. Mofijur, Advancing energy storage: The future trajectory of lithium-ion battery technologies, J. Energy Storage 120 (2025) http://dx.doi.org/10.1016/j.est.2025.116511.

[10] L. Zhao, T. Zhang, W. Li, T. Li, L. Zhang, X. Zhang, Z. Wang, Engineering of sodium-ion batteries: Opportunities and challenges, Engineering 24 (2023) http://dx.doi.org/10.1016/j.eng.2021.08.032.

[11] R. Wanison, W.N.H. Syahputra, N. Kammuang-lue, P. Sakulchangsatjatai, C. Chaichana, V.U. Shankar, P. Suttakul, Y. Mona, Engineering aspects of sodium-ion battery: An alternative energy device for lithium-ion batteries, J. Energy Storage 100 (2024) http://dx.doi.org/10.1016/j.est.2024.113497.

[12] T.F. Qahtan, I.O. Alade, A. AlArjani, M.S. Rahaman, Advancements in sodium-ion batteries: An in-depth scientometric review, J. Energy Storage 131 (2025) http://dx.doi.org/10.1016/j.est.2025.117490.

[13] A. Yao, S.M. Benson, W.C. Chueh, Critically assessing sodium-ion technology roadmaps and scenarios for techno-economic competitiveness against lithium-ion batteries, Nat. Energy 10 (2025) http://dx.doi.org/10.1038/s41560-024-01701-9.

[14] M. Li, Elevating the practical application of sodium-ion batteries through advanced characterization studies on cathodes, Energies 16 (2023) http://dx.doi.org/10.3390/en16248004.

[15] V. Marangon, K. Bischof, A.A. Regalado, M. Keppeler, M. Pogosova, M. Wan, J. Choi, S. Fleischmann, T. Diemant, M. Wohlfahrt-Mehrens, M. Hölzle, T. Waldmann, D. Bresser, Cell design and chemistry of commercial sodium-ion battery cells, J. Power Sources 634 (2025) http://dx.doi.org/10.1016/j.jpowsour.2025.236496.

[16] M. Rehm, M. Fischer, M.R. Gomez, M. Schütte, D.U. Sauer, A. Jossen, Comparing the electrical performance of commercial sodium-ion and lithium-iron-phosphate batteries, J. Power Sources 633 (2025) http://dx.doi.org/10.1016/j.jpowsour.2025.236290.

[17] H. Laufen, S. Klick, H. Ditler, K.L. Quade, A. Mikitisin, A. Blömeke, M. Schütte, D. Wasylowski, M. Sonnet, L. Henrich, A. Schwedt, G. Stahl, F. Ringbeck, J. Mayer, D.U. Sauer, Multi-method characterization of a commercial 1.2 Ah sodium-ion battery cell indicates drop-in potential, Cell Rep. Phys. Sci. 5 (2024) http://dx.doi.org/10.1016/j.xcrp.2024.101945.

[18] E. Irujo, A. Berrueta, P. Sanchis, A. Ursúa, Experimental characterization and aging analysis of commercial 18650 sodium-ion cells, in: 2024 International Conference on Renewable Energies and Smart Technologies, REST 2024, 2024, http://dx.doi.org/10.1109/REST59987.2024.10645381.

[19] E. Irujo, A. Berrueta, P. Sanchis, A. Ursúa, Methodology for comparative assessment of battery technologies: Experimental design, modeling, performance indicators and validation with four technologies, Appl. Energy 378 (2025) http://dx.doi.org/10.1016/j.apenergy.2024.124757.

[20] T. Waldmann, A. Iturrondobeitia, M. Kasper, N. Ghanbari, F. Aguesse, E. Bekaert, L. Daniel, S. Genies, I.J. Gordon, M.W. Löble, E.D. Vito, M. Wohlfahrt-Mehrens, Review—Post-mortem analysis of aged lithium-ion batteries: Disassembly methodology and physico-chemical analysis techniques, J. Electrochem. Soc. 163 (2016) http://dx.doi.org/10.1149/2.1211609jes.

[21] K. Nováková, A. Berrueta, A. Soto, P. Sanchis, A. Ursúa, Impact of micro-cycles on the lifetime of lithium-ion batteries - EIS analysis, in: 2024 IEEE 22nd Mediterranean Electrotechnical Conference, MELECON 2024, Institute of Electrical and Electronics Engineers Inc., 2024, http://dx.doi.org/10.1109/MELECON56669.2024.10608669.

[22] Z. Xu, H. Li, M. Yazdi, K. Ouyang, W. Peng, Aging characteristics and state-of-health estimation of retired batteries: An electrochemical impedance spectroscopy perspective, Electron. (Switz.) 11 (2022) http://dx.doi.org/10.3390/electronics11233863.

[23] E. Braco, I.S. Martin, P. Sanchis, A. Ursúa, D.I. Stroe, Health indicator selection for state of health estimation of second-life lithium-ion batteries under extended ageing, J. Energy Storage 55 (2022) http://dx.doi.org/10.1016/j.est.2022.105366.

[24] S. Dai, Y. Tu, L. Yan, Y. Li, M. Ma, R. Huang, X. Yao, H. Pan, Observation and suppression of metallic and metallic-like plating on hard carbon for high-performance sodium-ion batteries, Mater. Today Energy 44 (2024) http://dx.doi.org/10.1016/j.mtener.2024.101605.

[25] K. Bischof, M. Feinauer, A.A. Regalado, M. Wohlfahrt-Mehrens, M. Hölzle, T. Waldmann, Sodium metal deposition in commercial sodium-ion cells, J. Electrochem. Soc. 172 (2025) http://dx.doi.org/10.1149/1945-7111/ae0075.

[26] Tycorun Energy, 2024, www.takomabattery.com.

[27] M. Schütte, H. Laufen, D. Luder, H. Ditler, J. Kern, S. Klick, M. Junker, G. Stahl, F. Frie, D.U. Sauer, First full cell parameterization of a commercial layered oxide/hard carbon sodium-ion 18650 battery cell for a physico-chemical model, J. Energy Storage 107 (2025) http://dx.doi.org/10.1016/j.est.2024.114931.

[28] A. Reiter, M. Schütte, C. Rosenmüller, F. Stroebl, S. Lehner, D.U. Sauer, O. Bohlen, Exploring the effects of aging, temperature and hysteresis on the entropy variation of lithium-ion batteries, J. Energy Storage 140 (2025) http://dx.doi.org/10.1016/j.est.2025.118897.

[29] B.Y. Chang, Conversion of a constant phase element to an equivalent capacitor, J. Electrochem. Sci. Technol. 11 (2020) http://dx.doi.org/10.33961/jecst.2020.00815.

[30] M. Ono, M. Takahashi, R. Tamura, S. Matsuda, Unveiling electrolyte design principles for sodium-ion batteries using combinatorial electrochemistry and machine learning-assisted analysis, ACS Appl. Energy Mater. 9 (2026) http://dx.doi.org/10.1021/acsaem.5c03028.

[31] C. Jiang, Y. Wang, Z. Sun, Z. Chen, Fractional-order equivalent circuit model for commercial sodium-ion batteries in a wide temperature range considering aging, J. Energy Storage 105 (2025) http://dx.doi.org/10.1016/j.est.2024.114552.

[32] Z. Ahmad, V. Venturi, H. Hafiz, V. Viswanathan, Interfaces in solid electrolyte interphase: Implications for lithium-ion batteries, J. Phys. Chem. C 125 (2021) http://dx.doi.org/10.1021/acs.jpcc.1c00867.

[33] F.A. Soto, A. Marzouk, F. El-Mellouhi, P.B. Balbuena, Understanding ionic diffusion through SEI components for lithium-ion and sodium-ion batteries: Insights from first-principles calculations, Chem. Mater. 30 (2018) http://dx.doi.org/10.1021/acs.chemmater.8b00635.

[34] R. Liu, D.C. Sinclair, A.R. West, Electrochemical impedance spectroscopy of battery systems, including sodium materials, Curr. Opin. Electrochem. 55 (2026) http://dx.doi.org/10.1016/j.coelec.2025.101800.

[35] N. Meddings, M. Heinrich, F. Overney, J.S. Lee, V. Ruiz, E. Napolitano, S. Seitz, G. Hinds, R. Raccichini, M. Gaberšček, J. Park, Application of electrochemical impedance spectroscopy to commercial Li-ion cells: A review, J. Power Sources 480 (2020) http://dx.doi.org/10.1016/j.jpowsour.2020.228742.

[36] A. Piccardi, S. Pettinato, M.C. Rossi, M. Girolami, S. Salvatori, Low-frequency measurements in electrochemical impedance spectroscopy: A brief review, Electron. (Switz.) 14 (2025) http://dx.doi.org/10.3390/electronics14204048.

[37] Q. Zhang, D. Wang, B. Yang, H. Dong, C. Zhu, Z. Hao, An electrochemical impedance model of lithium-ion battery for electric vehicle application, J. Energy Storage 50 (2022) http://dx.doi.org/10.1016/j.est.2022.104182.

[38] Y. Tian, C. Lin, H. Li, J. Du, R. Xiong, Detecting undesired lithium plating on anodes for lithium-ion batteries – A review on the in-situ methods, Appl. Energy 300 (2021) http://dx.doi.org/10.1016/j.apenergy.2021.117386.

[39] T.P. Heins, N. Schlüter, U. Schröder, Electrode-resolved monitoring of the ageing of large-scale lithium-ion cells by using electrochemical impedance spectroscopy, ChemElectroChem 4 (2017) http://dx.doi.org/10.1002/celc.201700686.

[40] T. Momma, M. Matsunaga, D. Mukoyama, T. Osaka, Ac impedance analysis of lithium ion battery under temperature control, J. Power Sources 216 (2012) http://dx.doi.org/10.1016/j.jpowsour.2012.05.095.

[41] A. Soto, A. Berrueta, I. Oficialdegui, P. Sanchis, A. Ursúa, Noninvasive aging analysis of lithium-ion batteries in extreme cold temperatures, IEEE Trans. Ind. Appl. 58 (2022) http://dx.doi.org/10.13039/501100011033.

[42] A. Mikitisin, H. Ditler, M. Schütte, Correlative electron and X-ray microscopy: a new lens for sodium-ion battery research, Methods Microsc. 2 (2025) http://dx.doi.org/10.1515/mim-2025-0008.